Thermoelectric properties of Fe and Al double substituted MnSiγ (γ~1.73)

Journal of Solid State Chemistry 227 (2015) 55–59

Contents lists available at ScienceDirect

Journal of Solid State Chemistry

journal homepage: www.elsevier.com/locate/jssc

Thermoelectric properties of Fe and Al double substituted $MnSi_\gamma$ ($\gamma \sim 1.73$)

S.A. Barczak [a], R.A. Downie [a], S.R. Popuri [a], R. Decourt [b,c], M. Pollet [b,c], J.W.G. Bos [a,*]

[a] Institute of Chemical Sciences and Centre for Advanced Energy Storage and Recovery, School of Engineering and Physical Sciences, Heriot-Watt University, Edinburgh EH14 4AS, UK
[b] CNRS, ICMCB, UPR 9048, Pessac F-33600, France
[c] Univ. Bordeaux, ICMCB, UPR 9048, Pessac, F-33600, France

ARTICLE INFO

Article history:
Received 9 October 2014
Received in revised form
16 March 2015
Accepted 17 March 2015
Available online 26 March 2015

Keywords:
Nowotny chimney ladder phase
Higher manganese silicide
Thermoelectric energy conversion

ABSTRACT

Two series of Fe and Al double substituted $MnSi_\gamma$ chimney ladders with a nominal valence electron count, VEC = 14 per transition metal were prepared ($\gamma = 1.75$). Simultaneous replacement of Mn with Fe and Si with Al yielded the $Mn_{1-x}Fe_xSi_{1.75-x}Al_x$ series while the second $Mn_{1-x}Fe_xSi_{1.75-1.75x}Al_{2x}$ series follows the pseudo-binary between $MnSi_{1.75}$ and $FeAl_2$. Scanning electron microscopy and elemental mapping revealed that ~60% of the nominal Al content ends up in the product with the remainder lost to sublimation, and that up to 7% Al can be substituted in the main group sublattice. Profile analysis of X-ray powder diffraction data revealed gradual changes in the cell metrics, consistent with the simultaneous substitution of Fe and Al in a fixed ratio. All samples are p-type with VEC ≈ 13.95 from the structural data and $\sim 1 \times 10^{21}$ holes cm^{-3} from variable temperature Seebeck measurements. The substituted samples have lower electrical resistivities ($\rho_{300\,K}$ = 2–5 mΩ cm) due to an improved microstructure. This leads to increased thermoelectric power factors (largest $S^2/\rho = 1.95$ mW m^{-1} K^{-2}) compared to $MnSi_\gamma$. The thermal conductivity for the $Mn_{0.95}Fe_{0.05}Si_{1.66}Al_{0.1}$ sample is 2.7 W m^{-1} K^{-1} between 300 and 800 K, and is comparable to literature data for the parent material.

1. Introduction

Thermoelectric energy converters can be used to increase the efficiency of any heat generating process. However, the lack of cost-effective thermoelectric materials has so far limited their use to certain niche applications [1]. The efficiency of a thermoelectric material is defined by its dimensionless figure of merit, $ZT = (S^2/\rho\kappa)T$, where S is the Seebeck coefficient, ρ is the electrical resistivity, $\kappa = \kappa_{el} + \kappa_{lat}$ is the sum of the electronic and lattice thermal conductivities, and T is the absolute temperature [1]. Over the past decades a large number of material systems have been investigated for thermoelectric power generation, including lead tellurides, skutterudites, half-Heuslers and silicon-germanium alloys [2–6]. Another group of materials under investigation are intermetallic compounds with the Nowotny chimney-ladder (NCL) structure. These form for a variety of combinations of group 4–9 transition metals and group 13–14 main group elements with VEC ≈ 14 [7–10]. When the VEC is close to 14, the Fermi energy is located in the middle of a narrow band gap and the chimney ladder compounds exhibit semiconducting properties.

In particular, manganese silicides with composition $MnSi_\gamma$ ($1.70 \le \gamma \le 1.75$) have attracted significant interest because of their promising ZT = 0.5 but also because of their low cost, environmental friendliness, chemical and mechanical stability and resistance to oxidation at high temperatures [11,12]. The $MnSi_\gamma$ structure consists of two tetragonal subsystems: a [Mn] chimney and a [Si] ladder which share a common a axis but have different and often incommensurate repeat periods along the c-direction. A convenient structural description uses a 3+1 dimensional model (superspace group $I4_1/amd(00\gamma)00ss$) consisting of a basic tetragonal cell $a \times a \times c_{Mn}$ ($a \approx 5.5$ Å, $c_{Mn} \approx 4.4$ Å) and a modulation parameter ($\gamma = c_{Mn}/c_{Si}$) [12,13]. Because both [Mn] and [Si] subsystems contain exactly 4 atoms, by defining γ, it is possible to obtain the experimental stoichiometry of the material. $MnSi_\gamma$ compositions with the NCL structure are traditionally known as the higher manganese silicides, and were initially considered to only exist for special Mn:Si ratios. For example, Mn_4Si_7 ($\gamma = 1.75$) [14], $Mn_{27}Si_{47}$ ($\gamma = 1.741$) [15], $Mn_{15}Si_{26}$ ($\gamma = 1.733$) [16] and $Mn_{11}Si_{19}$ ($\gamma = 1.727$) [17] were all reported as commensurate structures with long c axes. However, the modulated structure description suggests that an infinitely adaptive series with gradually changing periodicity exists for $1.70 \le \gamma \le 1.75$.

Uncertainty often exists in the literature regarding the main group content but $MnSi_\gamma$ is usually p-type, suggesting that the

* Corresponding author.
E-mail address: j.w.g.bos@hw.ac.uk (J.W.G. Bos).

http://dx.doi.org/10.1016/j.jssc.2015.03.017

experimental $\gamma < 1.75$ (VEC < 14), despite starting compositions that use as large values as $\gamma = 1.8$ (VEC = 14.2). Typical ZT values for the parent materials are 0.3–0.4 at 800 K [12], while recently ZT = 0.5 was reported for $MnSi_\gamma$ grown using vapour transport [18]. A large number of chemical substitutions have been reported for $MnSi_\gamma$. Most of these focus on the transition metal sublattice and include $Mn_{1-x}Fe_xSi_\gamma$ (ZT = 0.45 at 800 K) [19,20], $Mn_{1-x}Cr_xSi_\gamma$ (ZT = 0.45 at 900 K) [20–22], co-doping with Cr and Ru (ZT = 0.6 at 850 K) [21], $Mn_{1-x}Ru_xSi_\gamma$ (ZT = 0.75 at 875 K for $x = 0.1$) [23,24] and $Mn_{1-x}Re_xSi_\gamma$ (ZT = 0.6 at 800 K) [25]. Substitutions into the main group sublattice have also been explored, and in particular hole doping using Al has been found to be a promising route towards obtaining good figures of merit (e.g. ZT = 0.65 at 850 K) [26,27]. Germanium has been used to improve the power factor (S^2/ρ) [28], and simultaneous substitution of Al and Ge has been reported recently (ZT = 0.6 at 823 K) [29]. In all these studies, relatively small amounts of substitution (< 1% Al and < 2% Ge) into the main group sublattice were reported before segregation was observed. In an attempt to achieve higher substitution levels we have exploited the co-doping of Fe and Al to maintain a constant VEC = 14. Two series of materials were prepared: the first ($Mn_{1-x}Fe_xSi_{1.75-x}Al_x$) was created by 1:1 substitution of Mn by Fe and Si by Al to maintain an overall $AX_{1.75}$ stoichiometry. The second series ($Mn_{1-x}Fe_xSi_{1.75-1.75x}Al_{2x}$) connects two binary phases that obey the VEC = 14 rule: $MnSi_{1.75}$ and $FeAl_2$. This series has an increasing main group to transition metal ratio ($AX_{1.75+0.25x}$). The structure and microstructure of these samples were investigated using X-ray powder diffraction and scanning electron microscopy and energy dispersive X-ray elemental (EDX) mapping, while the thermoelectric performance was determined through measurement S, σ and κ.

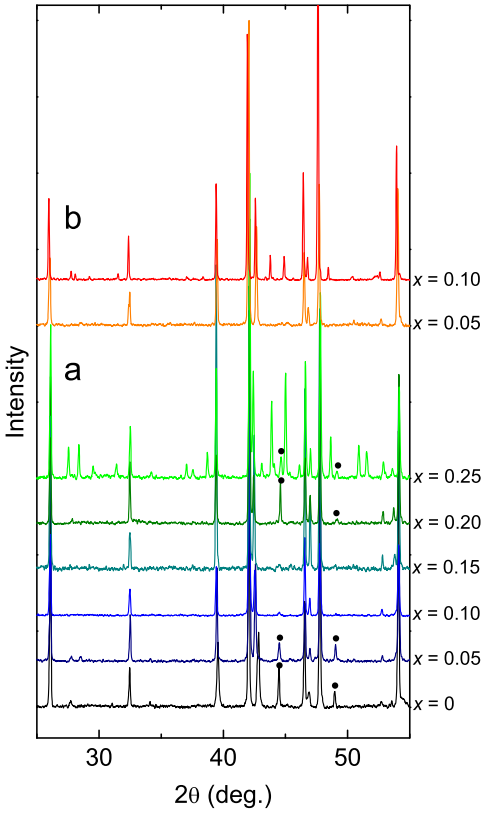

Fig. 1. X-ray powder diffraction patterns for Fe and Al double substituted $MnSi_{1.75}$: (a) the $Mn_{1-x}Fe_xSi_{1.75-x}Al_x$ series and (b) the $Mn_{1-x}Fe_xSi_{1.75-1.75x}Al_{2x}$ series. (● Denotes MnSi).

2. Experimental procedure

Three gram polycrystalline samples with nominal compositions $Mn_{1-x}Fe_xSi_{1.75-x}Al_x$ ($0 \le x \le 0.25$) and $Mn_{1-x}Fe_xSi_{1.75-1.75x}Al_{2x}$ ($0 \le x \le 0.1$) were synthesised by arc-melting and annealing. Stoichiometric amounts of Mn (99.6%), Fe (99.9+%), Si (99.99%) and Al (99.97%) were mixed using a mortar and pestle and pressed into 13 mm diameter pellets. The pellets were arc-melted on a water cooled copper plate under an argon atmosphere. Samples were melted 2 or 3 times and after each melting process they were flipped upside down in order to promote homogeneous mixing. The arc-melted ingots were subsequently wrapped in tantalum foil and annealed in evacuated, sealed quartz tubes at 900 °C for 5 days. A black residue coated the inside of the arc-melting chamber, while minor discoloration of the quartz tubes was observed after annealing. The overall weight loss was ≤2 wt%. X-ray powder diffraction patterns (XRD) were recorded to check the phase purity and determine the lattice parameters for all samples. Data were collected on a Bruker D8 Advance instrument with monochromated Cu$K\alpha_1$ radiation. The X-ray diffraction patterns were analysed using the JANA2006 software package [30]. The microstructure and chemical composition of a subset of the samples was analysed using a Quanta 650 FEG ESEM equipped with an Oxford Instruments X-max 150^N detector for elemental mapping. The working distance, beam spot size and collecting time were 10 mm, 4.5 and 4–10 frames, respectively. Prior to analysis the samples were polished using fine Al_2O_3 sand paper down to 0.5 μm roughness. Rectangular bars were cut using a diamond saw and used for transport measurements. High temperature (300–1100 K) measurements of S and ρ were carried out using a Linseis LSR-3 instrument. The thermal conductivity (κ) of the $Mn_{0.95}Fe_{0.05}Si_{1.662}Al_{0.1}$ sample was calculated from the measured thermal diffusivity α, specific heat capacity C_p, and density d using the relation $\kappa = \alpha C_p d$. The thermal diffusivity and heat capacity were measured using a Netzch LFA 457 and Perkin Elmer DSC 8500, respectively. The accuracy of the thermal conductivity is estimated to be ±7.5%. The sample densities were calculated from the mass and volume of the bars used in the transport measurements.

3. Results

3.1. Phase analysis

The powder XRD patterns of all samples are given in Fig. 1. Starting with the $AX_{1.75}$ series, the common impurity phase MnSi was observed for $x = 0$ and $x = 0.05$ and again at the highest substitution levels ($x = 0.2$ and 0.25). For $x = 0.25$ a new phase emerges in addition the NCL reflections. We have not been able to index this phase but it does not correspond to any known binary or ternary phase, including $FeAl_2$ for which a triclinic structure is reported [31,32]. The $AX_{1.75+0.25x}$ series with increasing main group content has a smaller substitution window and could only be prepared for $x = 0.05$ (0.1 Al). For $x = 0.1$, a second phase which is very similar in appearance to that observed in the $AX_{1.75}$ series is observed. The lattice parameters, volume of the basic cell and the main group content (γ) for the $Mn_{1-x}Fe_xSi_{1.75-x}Al_x$ and $Mn_{1-x}Fe_xSi_{1.75-1.75x}Al_{2x}$ series are shown in Fig. 2, and are listed in Table S1. Literature data for the $Mn_{1-x}Fe_xSi_\gamma$ series in which Mn is replaced by Fe, leading to electron doping, is included in Fig. 2 [19]. In this reference series, a shrinkage of the a- and c axes is observed. For the $AX_{1.75}$ series, a small reduction in the a axis and an almost constant c axis are observed, which is consistent with the simultaneous replacement of Mn with smaller Fe and Si with larger Al. The $AX_{1.75+0.25x}$ series has increasing lattice parameters, in keeping with the larger main group content. Both the $x = 0.25$ sample from the $AX_{1.75}$ series and the $x = 0.1$ sample from the $AX_{1.75+0.25x}$ series (open symbols in Fig. 2) follow the trends set by the pure samples without

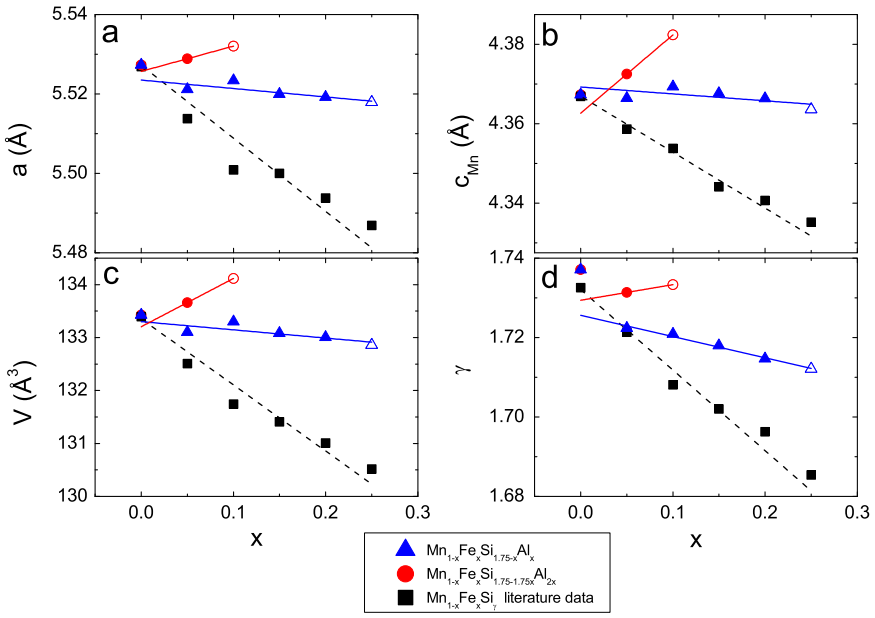

Fig. 2. Composition dependence of the basic cell parameters (a, c_{Mn}, and V) and the main group content (γ) for the $Mn_{1-x}Fe_xSi_{1.75-x}Al_x$ and $Mn_{1-x}Fe_xSi_{1.75-1.75x}Al_{2x}$ series. The reference data for the $Mn_{1-x}Fe_xSi_\gamma$ series were taken from Ref. [19]. Samples that contain the competing phase (see text) are represented by open symbols.

the competing phase, suggesting that the solubility limit may not be reached. The main group content (γ) for the $AX_{1.75}$ series decreases gradually upon Fe and Al substitution (Fig. 2). The main group content for the $AX_{1.75+0.25x}$ series is larger and is increasing, in keeping with the expected trend. Extrapolation towards $x=0$ suggests an estimated $\gamma=1.725$ for the $AX_{1.75}$ series, and $\gamma=1.730$ for the $AX_{1.75+0.25x}$ series. This reveals a subtle step change reduction in main group content compared to the $MnSi_{1.737}$ parent phase ($\Delta\gamma\approx-0.01$).

Scanning electron microscopy and elemental mapping were used to investigate the microstructure and chemical compositions for the samples upon which property measurements were undertaken. These are: $MnSi_{1.75}$, $x=0.1$ and 0.2 from the $AX_{1.75}$ series and $x=0.05$ from the $AX_{1.75+0.25x}$ series. The results are summarised in Fig. 3 and Table 1. The $MnSi_{1.75}$ sample has the most surface structure while the other samples appear better sintered, and had a better finish after polishing. Elemental mapping for $MnSi_{1.75}$ (not shown) showed a homogenous distribution of Mn and Si, and also revealed small amounts of elemental Si impurities not evident from the X-ray powder diffraction. An average of three large area elemental maps (212×146 μm^2) taken on different phase pure regions of the ingot yielded a chemical composition $MnSi_{1.67(3)}$, where the standard deviation is the variation between the three datasets. Similar analysis on homogenous areas of the Fe and Al substituted samples yielded the following chemical compositions: $Mn_{0.90}Fe_{0.098(7)}Si_{1.60(1)}Al_{0.063(7)}$, $Mn_{0.80}Fe_{0.18(1)}Si_{1.48(2)}Al_{0.11(1)}$, and $Mn_{0.95}Fe_{0.049(1)}Si_{1.64(1)}Al_{0.059(2)}$. The transition metal content is therefore in excellent agreement with the nominal values, while the total main group content is systematically underestimated. In terms of Al content, the EDX data consistently suggest this is ~60% of the expected content for both series. This large reduction is consistent with the weight loss observed during arc-melting (≤2 wt%) which is sufficient to explain the loss assuming Al is preferentially sublimated. A similar loss of Al was observed during directional solidification of $Ru_{0.27}Re_{0.73}(Si_{1-x}Al_x)_{1.67}$ alloys [33], and this may be a general feature of materials prepared from the melt. The elemental mapping also picked up residual Al-rich areas in the ingots but these are small and are not sufficient to explain the ~40% loss. In addition, there is no evidence for the presence of elemental Al in the X-ray powder diffraction data. The Al-rich areas are often linked to porosity in the microscopy images (see Fig. 3b). The $Mn_{0.80}Fe_{0.18(1)}Si_{1.48(2)}Al_{0.11(1)}$ sample is characterised by a large number of pores with diameters up to 50 μm while the areas in between are well sintered and of homogeneous chemical composition (Fig. 3d). This suggests that the subliming Al (melting point 660 °C) serves as a mineraliser promoting sintering but also leads to the presence of porosity due to trapped Al vapour. The competition between improved sintering and porosity is also reflected in the sample densities (Table 1) with the highest values observed for the samples with a nominal amount of 0.1 Al per formula unit.

3.2. Thermoelectric properties

The temperature dependence of S, ρ and S^2/ρ for $MnSi_{1.75}$, $x=0.1$ and 0.2 from the $AX_{1.75}$ series and $x=0.05$ from the $AX_{1.75+0.25x}$ series are given in Fig. 4. The observed $S(T)$ are positive and are characterised by a linear increase up to a broad maximum at 700–800 K, beyond which S is reduced. This behaviour is typical for degenerate semiconductors with a contribution from minority carriers (n-type) at higher temperatures. The linear part of $S(T)$ suggests a fixed number of charge carriers and was fitted using $S=(8\pi^2k_B^2/3eh^2)m^*(\pi/3n)^{2/3}T$ [2], where k_B is Boltzmann's constant, e is the electronic charge, h is Planck's constant, m^* is the effective mass and n is the carrier concentration. The carrier concentrations are in the range of $1–1.4\times10^{21}$ cm^{-3} (Table 1) using a hole effective mass of three times the bare electron mass [34]. The thermal band gaps (E_g) were estimated using $E_g=2eS_{max}T_{max}$ where S_{max} and T_{max} are the maximum Seebeck coefficient and the temperature at which it occurs [35]. Band gap values of 0.38 eV were found for all compositions (Table 1). The $\rho(T)$ data also show a linear increase up to a maximum which occurs at slightly higher temperatures (700–900 K) compared to the maximum in $S(T)$. This again reflects the contribution of minority charge carries at elevated temperatures. The most striking feature of the $\rho(T)$ data is the scatter in magnitude, which varies between 2 and 10 mΩ cm at room temperature. Given the similar $S(T)$ these variations cannot be due to changes in carrier concentration but must reflect microstructure factors. The microscopy data suggest that Al acts as a mineraliser leading to improved sintering which is expected to remove grain boundary contributions to the electrical transport. The presence of porosity due to trapped Al vapour is not expected to affect $\rho(T)$ significantly as the concentration of pores

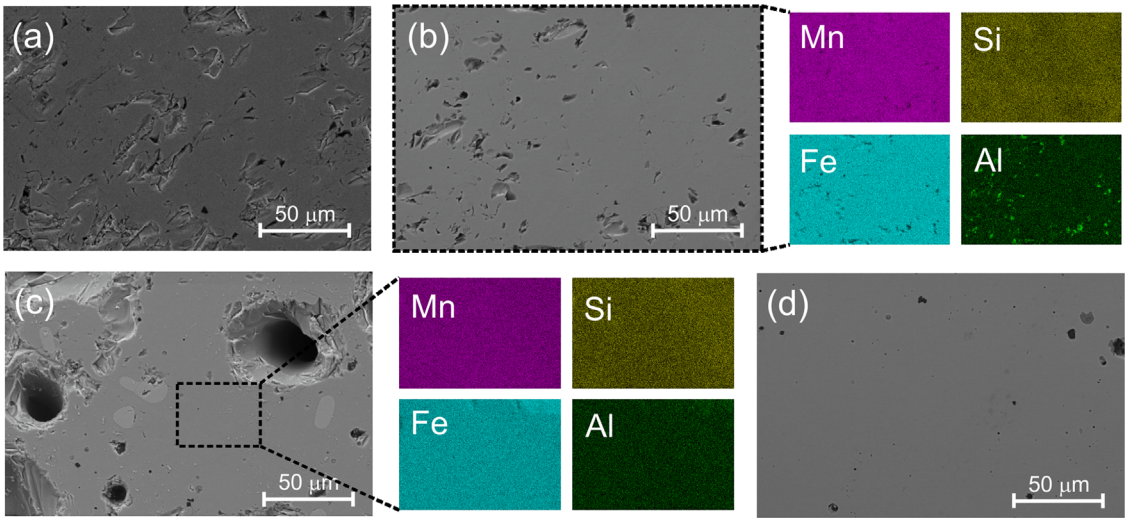

Fig. 3. Composite backscattered and secondary electron SEM images and EDX elemental maps for (a) $MnSi_{1.75}$, (b) $Mn_{0.9}Fe_{0.1}Si_{1.65}Al_{0.1}$, (c) $Mn_{0.8}Fe_{0.2}Si_{1.55}Al_{0.2}$, and (d) $Mn_{0.95}Fe_{0.05}Si_{1.662}Al_{0.1}$. The areas and collection times for the EDX maps are 212 × 146 μm² and 8 frames for (b) and 53.1 × 36.5 μm² and 4 frames for (c). All elemental maps contain 1024 × 704 pixels. The light areas in part (c) correspond to MnSi.

Table 1
EDX composition, total main group content (γ), valence electron count, density, resistivity (ρ) and Seebeck coefficient (S) at 315 K, thermal band gaps (E_g) and carrier concentrations (n_p) for selected $Mn_{1-x}Fe_xSi_{1.75-x}Al_x$ and $Mn_{1-x}Fe_xSi_{1.75-1.75x}Al_{2x}$ compositions.

x	EDX composition	γ	VEC	Density (g cm^{-3})	$\rho_{315\ K}$ (mΩ cm)	$S_{315\ K}$ (μV K^{-1})	E_g (eV)	n_p (10^{21} cm^{-3})
0	$MnSi_{1.67(3)}$	1.737	13.95	4.76	10.4	105	0.38	1.0
0.1	$Mn_{0.90}Fe_{0.098(7)}Si_{1.60(1)}Al_{0.063(7)}$	1.721	13.92	4.91	2.0	127	0.38	1.2
0.2	$Mn_{0.80}Fe_{0.18(1)}Si_{1.48(2)}Al_{0.11(1)}$	1.715	13.94	4.53	5.2	136	0.38	1.0
0.05 ($AX_{1.75+0.25x}$)	$Mn_{0.95}Fe_{0.049(1)}Si_{1.64(1)}Al_{0.059(2)}$	1.731	13.91	4.92	3.6	121	0.38	1.4

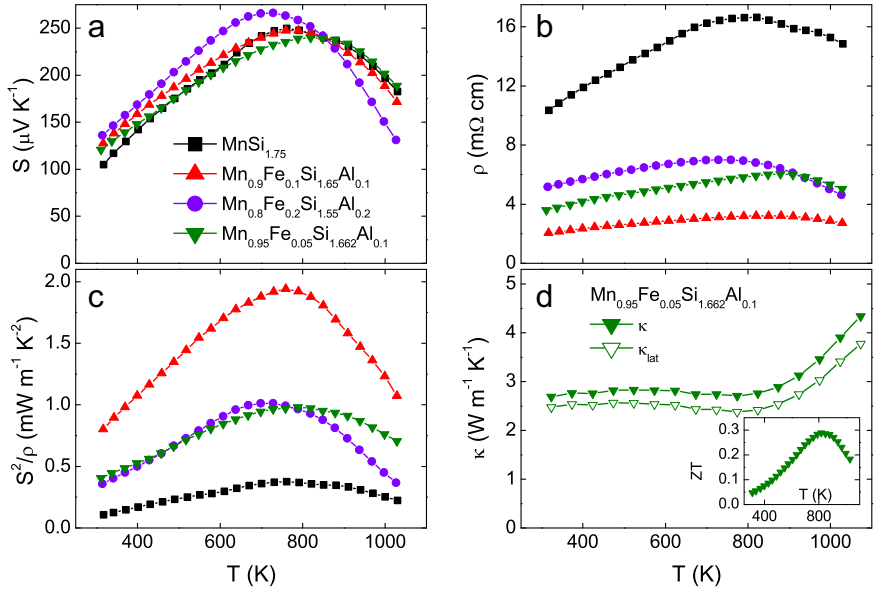

Fig. 4. Temperature dependence of (a) the Seebeck coefficient (S), (b) the electrical resistivity (ρ), (c) the power factor (S^2/ρ) for a subset of the $Mn_{1-x}Fe_xSi_{1.75-x}Al_x$ and $Mn_{1-x}Fe_xSi_{1.75-1.75x}Al_{2x}$ samples. Part (d) shows the total (κ) and lattice (κ_{lat}) thermal conductivity for $Mn_{0.95}Fe_{0.05}Si_{1.662}Al_{0.10}$. The inset shows the figure-of-merit (ZT) for $Mn_{0.95}Fe_{0.05}Si_{1.662}Al_{0.10}$.

remains low. Indeed, all substituted samples have significantly lowered $\rho(T)$ values ($2 < \rho_{300\ K} < 5$ mΩ cm) compared to the parent material ($\rho_{300\ K} = 10$ mΩ cm), in keeping with a reduction of grain boundary contributions. The temperature dependence of S^2/ρ is similar for all samples with a broad maximum centred on 700–800 K. The variation in magnitude is accounted for by the observed scatter in $\rho(T)$. A maximum $S^2/\rho = 1.9$ mW m^{-1} K^{-2} is observed for the $x = 0.1$ sample from the $AX_{1.75}$ series. The $\kappa(T)$ of the $x = 0.05$ sample from the $AX_{1.75+0.25x}$ series was measured as a representative sample. The $\kappa(T)$ is almost temperature independent up to 800 K ($\kappa = 2.7$ W m^{-1} K^{-1}) beyond which it increases rapidly (Fig. 4d). This sudden increase is linked to a bipolar contribution due to the presence of both p- and n-type charge carriers. It is therefore not possible to extract a reliable lattice thermal conductivity using the normal subtraction of a

Wiedemann–Franz term over the entire temperature range. At low temperatures, where p-type carriers dominate, a reasonable estimate for κ_{lat} can be obtained from $\kappa - LT/\rho$ with $L = 2.45 \times 10^{-8}$ V^2 K^{-2}. The calculated κ_{el} are on the order of 0.2–0.4 W m^{-1} K^{-1} and therefore are only a minor component of the total κ. The room temperature value for $\kappa_{lat} = 2.5$ W m^{-1} K^{-1} which is comparable to literature values for $MnSi_\gamma$ ($\gamma \sim 1.75$) samples without chemical substitutions [18,19].

4. Discussion

X-ray powder diffraction and microscopy imaging confirm that Fe and Al double substitution is an effective route to increase the amount of Al substitution in the $MnSi_\gamma$ chimney ladder structure. EDX elemental analysis suggests that about 60% of the nominal Al content is found in the final product while the remainder is lost due to sublimation. This constant percentage loss is supported by the systematic changes in the cell metrics which suggest successful co-doping of Fe and Al in a fixed ratio. The highest substitution level is 7% of the main group lattice, and was observed for the $x = 0.2$ sample of the $Mn_{1-x}Fe_xSi_{1.75-x}Al_x$ series. The measured S(T) are nearly identical and demonstrate that all samples have similar carrier concentrations. The lack of significant doping suggests that the Si/Al ratio and total main group content (γ) adjust to maintain a carrier concentration close to that of the parent material (VEC = 13.95). This is confirmed by taking the Si/Al ratio from EDX and the total main group content (γ) from diffraction and calculating the VEC for the substituted samples (Table 1). This leads to VEC = 13.92 ($x = 0.1$; $AX_{1.75}$ series), VEC = 13.94 ($x = 0.2$; $AX_{1.75}$ series) and VEC = 13.91 ($x = 0.05$, $AX_{1.75+0.25x}$ series). This suggests that the changes in Si/Al ratio and γ are purely driven by electronic origins, and may not be caused by the rapid nature of the arc-melting process itself. For both series a competing phase was observed as x was increased, signalling that there is a limit to the amount of Al (~7% from our EDX data) that can be incorporated in the NCL structure. To test whether the presence of Al is the limiting factor in the phase stability, the two-phase $x = 0.25$ sample from the $AX_{1.75}$ series was prepared with a gradually decreasing Al content. This yielded the $Mn_{0.75}Fe_{0.25}Si_{1.6875-0.75y}Al_y$ series ($0 \le y \le 0.25$) whose X-ray powder diffraction patterns and lattice parameters are given in Figs. S2–S3 and Table S2. Inspection of the diffraction data reveals that the replacement of Al with Si eliminates the competing phase for $y \le 0.1$. This suggests that the presence of Al is indeed the limiting factor in the phase stability of these materials. The electron microscopy, sample densities and variations in $\rho(T)$ all suggest that Al serves as a mineraliser leading to improved sintering but also to porosity due to trapped vapour. This leads to $\rho(T)$ and S^2/ρ values for $Mn_{0.9}Fe_{0.1}Si_{1.65}Al_{0.1}$ that are comparable to the best reported $MnSi_\gamma$ based materials [18,26]. Elimination of the porosity due to trapped Al vapour may enable further improvements in $\rho(T)$ and S^2/ρ. The inset to Fig. 4d shows the temperature dependence of ZT for the $x = 0.05$ sample from the $AX_{1.75+0.25x}$ series, and this shows a maximum $ZT = 0.3$ at 825 K. Assuming a similar $\kappa(T)$ for the sample with the largest S^2/ρ values, leads to an estimated $ZT = 0.5$.

To conclude, double substitution of Fe and Al is a route to increase the Al content in the $MnSi_\gamma$ chimney ladder structure. The maximum observed Al content is 7% of the total main group sublattice. The prepared samples adjust their Si/Al ratio and total main group content (γ) in order to maintain a constant valence electron count near 13.95 electrons per formula unit. In terms of the thermoelectric performance, the Al substituted samples have improved electrical resistivities and power factors up to 1.95 mW m^{-1} K^{-2} are observed for a nominal $Mn_{0.9}Fe_{0.1}Si_{1.65}Al_{0.1}$ sample at 800 K.

Acknowledgments

We acknowledge the EPSRC (EP/J000884/1 and EP/K036408/1), Leverhulme Trust (RPG-2012-576) and Royal Society for support, and Jim Buckman, Institute of Petroleum Engineering, Heriot-Watt University, for his help during collection of the SEM-EDX data.

Appendix A. Supporting information

Supplementary data associated with this article can be found in the online version at http://dx.doi.org/10.1016/j.jssc.2015.03.017.

References

[1] D.M. Rowe, CRC Press, Boca Raton, FL, 2006.
[2] G.J. Snyder, E.S. Toberer, Nat. Mater. 7 (2008) 105–114.
[3] J.R. Sootsman, D.Y. Chung, M.G. Kanatzidis, Angew. Chem. Int. Ed. 48 (2009) 8616–8639.
[4] P. Vaqueiro, A.V. Powell, J. Mater. Chem. 20 (2010) 9577–9584.
[5] M. Zebarjadi, K. Esfarjani, M.S. Dresselhaus, Z.F. Ren, G. Chen, Energy Environ. Sci. 5 (2012) 5147–5162.
[6] J.W.G. Bos, R.A. Downie, J. Phys.—Condens. Matter 26 (2014) 433201.
[7] D.C. Fredrickson, S. Lee, R. Hoffmann, Inorg. Chem. 43 (2004) 6159–6167.
[8] D.C. Fredrickson, S. Lee, R. Hoffmann, J.H. Lin, Inorg. Chem. 43 (2004) 6151–6158.
[9] Y. Imai, A. Watanabe, Intermetallics 13 (2005) 233–241.
[10] V.J. Yannello, D.C. Fredrickson, Inorg. Chem. 53 (2014) 10627–10631.
[11] M.I. Fedorov, V.K. Zaitsev, in: D.M. Rowe (Ed.), Thermoelectric Handbook: Macro to Nano, CRC Press, Boca Raton, FL, 2006.
[12] Y. Miyazaki, Y. Kikuchi, in: K. Koumoto, T. Mori (Eds.), Thermoelectric Nanomaterials, Springer, Heidelberg, 2013.
[13] Y. Miyazaki, D. Igarashi, K. Hayashi, T. Kajitani, K. Yubuta, Phys. Rev. B 78 (2008) 214104.
[14] U. Gottlieb, A. Sulpice, B. Lambert-Andron, O. Laborde, J. Alloys Compd. 361 (2003) 13–18.
[15] G. Zwilling, H. Nowotny, Monatsh. Chem. 104 (1973) 668–675.
[16] H.W. Knott, M.H. Mueller, L. Heaton, Acta Crystallogr. 23 (1967) 549–555.
[17] O. Schwomma, H. Nowotny, A. Wittmann, Monatsh. Chem. 94 (1963) 681–685.
[18] S.N. Girard, X. Chen, F. Meng, A. Pokhrel, J.S. Zhou, L. Shi, S. Jin, Chem. Mater. 26 (2014) 5097–5104.
[19] Y. Miyazaki, Y. Saito, K. Hayashi, K. Yubuta, T. Kajitani, Jpn. J. Appl. Phys. 50 (2011) 035804.
[20] V. Ponnambalam, D.T. Morelli, J. Electron. Mater. 41 (2012) 1389–1394.
[21] V. Ponnambalam, D.T. Morelli, S. Bhattacharya, T.M. Tritt, J. Alloys Compd. 580 (2013) 598–603.
[22] Y. Kikuchi, Y. Miyazaki, Y. Saito, K. Hayashi, K. Yubuta, T. Kajitani, Jpn. J. Appl. Phys. 51 (2012) 085801.
[23] N.L. Okamoto, T. Koyama, K. Kishida, K. Tanaka, H. Inui, J. Electron. Mater. 39 (2010) 1640–1644.
[24] N.L. Okamoto, T. Koyama, K. Kishida, K. Tanaka, H. Inui, Acta Mater. 57 (2009) 5036–5045.
[25] X. Chen, S.N. Girard, F. Meng, E. Lara-Curzio, S. Jin, J.B. Goodenough, J.S. Zhou, L. Shi, Adv. Energy Mater. 4 (2014) 1400452.
[26] W.H. Luo, H. Li, F. Fu, W. Hao, X.F. Tang, J. Electron. Mater. 40 (2011) 1233–1237.
[27] D.K. Shin, S.W. You, I.H. Kim, J. Korean Phys. Soc. 64 (2014) 1412–1415.
[28] A.J. Zhou, T.J. Zhu, X.B. Zhao, S.H. Yang, T. Dasgupta, C. Stiewe, R. Hassdorf, E. Mueller, J. Electron. Mater. 39 (2010) 2002–2007.
[29] X. Chen, A. Weathers, D. Salta, L.B. Zhang, J.S. Zhou, J.B. Goodenough, L. Shi, J. Appl. Phys. 114 (2013) 173705.
[30] V. Petricek, M. Dusek, L. Palatinus, Z. Kristallogr. 229 (2014) 345–352.
[31] I. Chumak, K.W. Richter, H. Ehrenberg, Acta Crystallogr., Sect. C: Cryst. Struct. Commun. 66 (2010) 87–88.
[32] C.S. Lue, Y.K. Kuo, J. Phys. Condens. Matter 15 (2003) 877–882.
[33] K. Kishida, A. Ishida, T. Koyama, S. Harada, N.L. Okamoto, K. Tanaka, H. Inui, Acta Mater. 57 (2009) 2010–2019.
[34] D.B. Migas, V.L. Shaposhnikov, A.B. Filonov, V.E. Borisenko, N.N. Dorozhkin, Phys. Rev. B 77 (2008) 075205.
[35] H.J. Goldsmid, J.W. Sharp, J. Electron. Mater. 28 (1999) 869–872.